AIAA SciTech Forum
6-10 January 2020, Orlando, FL
AIAA Scitech 2020 Forum

10.2514/6.2020-0682

Turbulence Profiling Using AAOL-BC

Matthew Kalensky[1a], Yakov Diskin[2b], Matthew R. Whiteley[3b], Eric J. Jumper[4a], Richard Drye[b], Mitchell Grose[b], Kevin Jackovitz[b], Brandon Hampshire[b], Eric Smith[b], Aaron Archibald[c], Stanislav Gordeyev[a], Mike Zenk[a]

[a]*University of Notre Dame, Notre Dame, IN, USA, 46556*
[b]*MZA Associates Corporation, 1360 Technology Ct. Suite 200, Dayton, OH, USA, 45430*
[c]*Air Force Institute of Technology, 2950 Hobson Way, Wright-Patterson AFB, OH 45433*

AAOL-BC was employed to conduct experiments that seek to measure path resolved turbulence quantities. To explore the impact that atmospheric turbulence has on optical systems, a Path Resolved Optical Profiler System (PROPS) was employed. Ground-based and in-flight studies are conducted simultaneously and C_n^2 profiles are computed allowing the relationship between atmospheric turbulence strength and propagation path to be analyzed.

Nomenclature

C_n^2	= atmospheric refractive index structure parameter
H	= elevation above ground level
W	= high-altitude wind speed
A	= ground conditions input
σ_χ^2	= Rytov parameter
λ	= wavelength
L	= path length
σ_δ^2	= difference of differential tilt variances
d	= tilts
z	= position along path
a	= atmospheric tilt covariances
ξ	= normalized path position
$W(\xi)$	= weighting function
D	= aperture diameter
p	= weighting function matrix
r_0	= coherence length
α	= scaling factor
AGL	= above ground level

[1] Graduate Research Assistant, Department of Aerospace and Mech. Eng., Student AIAA Member
[2] Research Scientist, MZA Associates Corporation
[3] Vice President and Senior Scientist, MZA Associates Corporation
[4] Professor, Department of Aerospace and Mech. Eng., AIAA Fellow

I. Introduction

The propagation of a beam of light through an inhomogeneous medium distorts the initially unperturbed beam. The shape of the resultant distorted light wave is called a wavefront [1]. Propagation of light through the atmosphere has been of high interest due to its relevance in optical communication, imaging, and directed energy systems [2]. The random fluctuations of refractive index in the atmospheric medium are deleterious to the functionality and operation of these systems [2].

Recently, there has been extensive interest in the use of high energy laser systems mounted on a flight vehicle [3-9]. The use of airborne directed energy lasers offers great promise for next generation defense applications. The success of the Airborne Laser Laboratory (ALL) campaign in the 1970s and 1980s demonstrated the utility, as well as complexities of such a system [3]. A fully realized and operational airborne, high energy laser necessitates research into fundamental physics pertaining to beam aberration along the entirety of the propagation path. As research today gravitates towards implementing airborne directed energy systems capable of lethality on long-range targets, atmospheric turbulence effects are amplified and remain difficult to quantify. The work discussed here demonstrates how in-flight experimentation will quantify turbulence intensity along a slant path by propagating light through a turbulent atmosphere.

II. Background

A. Turbulence Theory and Profiling

C_n^2 is referred to as the atmospheric refractive index structure parameter and it is a measure of turbulence strength [2,10]. The physical roots of this parameter are derived from a well-accepted model of turbulence first proposed by Kolmogorov in the 1940s [2]. Due to the highly disordered space and time dependency of fluctuating fluid and optical parameters, current turbulence models are not derived from first principles [2]. Rather ad hoc theories were proposed based on physical observation and intuition in an effort to model these inherently complicated physical phenomena. These models utilize statistical approaches due to the lack of analytical solutions to turbulence problems. When the Reynolds number becomes high, as it does in these turbulent flows, even approximating the instantaneous flow field from a given set of initial conditions becomes virtually intractable. The theory proposed by Kolmogorov, centered around the idea of an "energy cascade," has laid the foundation for the turbulence modeling approaches currently used today [10]. Kolmogorov's formulation begins with the fact that the atmosphere is a viscous medium [2]. When a flow transitions from laminar to turbulent, the fluid loses its uniform nature due to mixing driven by wind shear and temperature gradients between the atmosphere and Earth's surface. Resultant local unstable air masses smaller in scale than the global flow form [2]. Energy injection occurs at the largest scales, and then due to dynamic mixing from the atmosphere's inertial forces, large scale turbulent structures are broken into smaller scale eddies until viscous forces become the preferential means for dissipation of energy [2,10]. Kolmogorov defined a range between large and small-scale structures in which the turbulence is statistically homogenous and isotropic [2,10]. This range was termed the "inertial subrange [2,11]." Here, stochastic models for turbulence modeling were proposed. The Kolmogorov theory of turbulence allows the random fluctuations of refractive index to abide by a level of statistical consistency within the inertial subrange, enabling parameters such as C_n^2 to be approximated [2,11].

Measuring C_n^2 at various positions along a path is typically referred to as "turbulence profiling [12]." For applications such as airborne lasers, optical communications, and imaging systems, an understanding of the turbulence environment that the light is propagating through is necessary. Atmospheric turbulence obstructs the spatial coherence of a laser beam as it is transmitted through the atmosphere, drastically hindering the degree that the laser can be focused on a target [2]. However, if the aberrations imposed on the optical wave are measurable, adaptive optics (AO) technology can compensate for the distortions and alleviate the undesirable effects. AO systems introduce a deformable mirror (DM) to adjust the phase of the outgoing laser beam, and a fast steering mirror (FSM) to compensate for the unsteady dynamic pointing, in an effort to maximize on-target power [14]. A thorough understanding of the turbulence encountered along a path is necessary for both design and accurate closed loop operation of an AO system [13,14]. The development of this technology is contingent on improved models and measurements of turbulence in the atmosphere.

B. Atmospheric Turbulence Models

In the past, it has been difficult to directly measure C_n^2 with reasonable confidence. Various attempts have been made using very high frequency (VHF) radar, scintillometers, isoplanometers, and thermosonde systems [15-20]. To further complicate calculation of this parameter, C_n^2 is continually changing, and depends on location, altitude, time of the day, wind, to name a few. Efforts have been made to develop a more concrete model to predict C_n^2 in the atmosphere. However, the dependence of C_n^2 on many variables makes modeling this parameter challenging. One of the current, widely used models for predicting C_n^2 is the Hufnagel-Valley Boundary model (HVB), as given in Eq. 1, where *h* is the elevation above ground level (AGL).

$$C_n^2(h) = 5.94x10^{-23}h^{10}e^{-h}\left(\frac{W}{27}\right) + 2.7x10^{-16}e^{-2h/3} + Ae^{-10h} \tag{1}$$

HVB only uses two input parameters, *W* and *A*. *W* is the approximate high-altitude wind speed and *A* is an input to account for near ground conditions. When *W* and *A* are taken to be 21 m/s and $1.7x10^{-14}$, respectively, this corresponds to a coherence length, r_0=5 cm and an isoplanatic angle, θ_0=7 μrad [21]. Fittingly, this specialized form of the model is referred to as *HV57*. With only two input parameters used for generating a C_n^2 approximation, the validity of this model and others alike is brought into question.

C. Difference of Differential Tilt Variances (DDTV)

Rytov theory is the primary basis for turbulence approximations resulting from optical wave propagation along a path [2,10,13]. The Rytov parameter, σ_χ^2, can be related to parameters such as C_n^2 by use of Eq. 2. Here, *z* is the position along the path and *L* is the full path length.

$$\sigma_\chi^2 = 0.5631\left(\frac{2\pi}{\lambda}\right)^{\frac{7}{6}}\int_0^L Cn^2(z)\left[z(1-\frac{z}{L})\right]^{\frac{5}{6}}dz \tag{2}$$

Eq. 2 is valid in propagation scenarios of weak turbulence. In instances of strong turbulence or for long propagation path lengths, scintillation saturates and Rytov theory can no longer be used to generate meaningful turbulence approximations [13,22]. With the amendable nature of Rytov theory for AO applications, we seek to extend the breadth of situations in which this theoretical construct can be applied. Rather than use irradiance-based quantities, the work described here utilizes DDTV, first outlined and presented in Ref. 12, to produce meaningful statistics to compute turbulence parameters. This method relies on phase related data, avoiding the issue of saturation. DDTV also avoids contamination from undesirable gimbal and noise motion [12]. The DDTV method utilizes an arbitrary number of sources and subapertures separated by the propagation path length of interest. The sources themselves are separated by a distance, *b*, considered small relative to the propagation path, *L*. On the side receiving the light from the sources, is a subaperture array where each subaperture is separated from the others by varying distances, Δ_x. The light from the sources is initially undisturbed. As the light wave propagates through the atmosphere, the small spatially and temporally dependent fluctuations in the atmosphere's refractive index perturb the light wave causing its departure from planarity. Using a Shack-Hartmann wavefront sensor (SHWFS), each subaperture focuses the light it receives from the sources to a point creating an

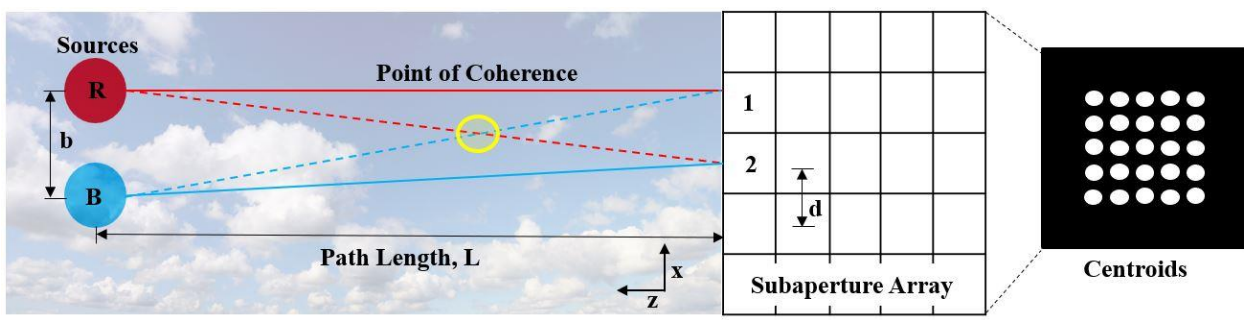

Figure 1. DDTV source and subaperture setup.

array of discrete illuminated spots, or centroids. The incoming light is filtered to observe the received light from each source. The *x* and *y* deviations, or tilts of these centroids away from their time resolved expected spatial locations is an indication of the incoming light sources, local deviation from planarity. The geometry of the source/aperture arrangement enables the existence of locations along the path where light emitted from the sources, crosses with the light received by different subaperture pairs. At these locations, there is coherence in how the optical waves are affected by the surrounding physical environment. Fig.1 illustrates the source/aperture schematic.

In this diagram, two light sources are used. A yellow circle highlights the location where the red and blue source light waves cross paths for a particular subaperture pair combination. Different subaperture pairs will yield a different point of coherence on the propagation path. Discrete locations of commonality allow the physical phenomena that occur along the entirety of the path to be approximated. Eq. 3 describes how the DDTV approach is applied from acquired tilt data.

$$\sigma_\delta^2 = \langle (d_{R1} - d_{B2})^2 \rangle - \langle (d_{R2} - d_{B1})^2 \rangle \tag{3}$$

In this equation, *d* represents the tilts for different subaperture/source combinations. *R* and *B* indicate which source the light is coming from. *1* and *2* represent the subapertures receiving the light source. Each tilt measurement can be broken into atmospheric, noise, and gimbal components. After expanding, simplifying, and ignoring the negligible components of Eq. 3, only the difference in atmospheric tilt covariances, *a*, remains. This result is shown in Eq. 4 [12].

$$\sigma_\delta^2 = 2(\langle a_{R2} a_{B1} \rangle - \langle a_{R1} a_{B2} \rangle) \tag{4}$$

For two subapertures separated by a physical distance, Δ_x, the covariance of Zernike x-tilt coefficients can be calculated using Eq. 5 [23,24,26]. The covariance for a specific $C_n^2(z)$ is a function of only normalized aperture and source separation. The $W(\xi)$ term represents a weighting function applied to the expression, *D* is the aperture diameter, and, λ is the wavelength. Eq. 5 can easily be substituted into the result determined from the DDTV geometry and with simplification, yields Eq. 6. This result produces an expression for the Rytov parameter that can be used to extract turbulence values for this geometry. Here, W_{0c} and W_0 are normalization constants and $w_c(\xi)$ and $w(\xi)$ are weighting functions for the cross path and non-cross path geometries, respectively. Eq. 6 reveals that DDTV generated quantities can be represented as a weighted integral of $C_n^2(z)$ [12]. If the known quantities in Eq. 6 are gathered into a quantity *m* as seen in Eq. 7, then Eq. 6 can be rearranged to form a linear system as seen in Eq. 8. Here, *p* is a matrix of weighting functions for *m* number of DDTV measurements by *n* number of propagation path partitions. Using the pseudo matrix inverse, C_n^2 can be calculated for partitions along the path. A more thorough explanation of the procedure and theoretical construct behind DDTV can be found in Ref. 12.

$$\langle a_1 a_2 \rangle = 16\sqrt{3}\Gamma(8/3) \left(\frac{2\pi}{\lambda}\right)^2 D^{\frac{5}{3}} L \int_0^L d\xi Cn^2(\xi L)\, W(\xi) \tag{5}$$

$$\sigma_\delta^2 = \frac{128\sqrt{3}\Gamma(8/3)}{\pi^2} \left(\frac{2\pi}{\lambda}\right)^2 D^{\frac{5}{3}} L \int_0^L d\xi Cn^2(\xi L)\, (W_{0c} w_c(\xi) - W_0 w(\xi)) \tag{6}$$

$$m_m = \frac{\sigma_\delta^2}{\frac{128\sqrt{3}\Gamma(\frac{8}{3})}{\pi^2} \left(\frac{2\pi}{\lambda}\right)^2 D^{5/3} LW} \tag{7}$$

$$\begin{bmatrix} m_1 \\ \vdots \\ m_M \end{bmatrix} = \begin{bmatrix} p_{11} & \cdots & p_{1N} \\ \vdots & \ddots & \vdots \\ p_{M1} & \cdots & p_{MN} \end{bmatrix} \begin{bmatrix} Cn_1^2 \\ \vdots \\ Cn_N^2 \end{bmatrix} \tag{8}$$

The curves shown in the left plot of Fig. 2 illustrate how different weights are applied along the propagation path based on the DDTV geometry. The solid blue curve represents the scenario in Fig. 1 where source *R* is received by aperture 1 and source *B* is received by aperture 2. The red dashed line in the left plot of Fig. 2 represents when source *R* is received by aperture 2 and source

B is received by aperture 1, otherwise referred to as the cross-path scenario. The point where the light from *R* and *B* intersect paths before being received by the subapertures is the point of coherence, shown in Fig. 1 at approximately ξ=0.3. At this intersection, both sources experience the same turbulence environment. Therefore, the resultant differential tilt variances are the same and the DDTV is zero. In the left plot of Fig. 2, the green path represents the difference between the non-cross and the cross-path weighting functions (DDTV) for one pair of source/subaperture combinations. Different subaperture pairs changes the location along the path where the sources intersect. Consequently, the point on the path where the weight is applied also changes. This method is applied to all possible source/subaperture combinations resulting in a more resolved path as seen in the right plot of Fig. 2.

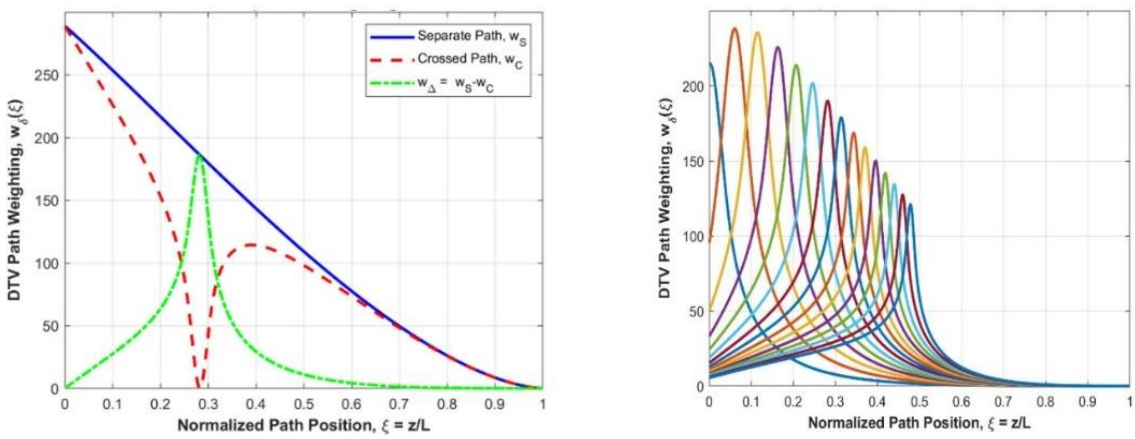

Figure 2. Left) Path weighting functions for one pair of subapertures. Right) Path weighting functions for multiple pairs of subapertures.

III. Experimental Setup

A. Airborne Aero-Optics Laboratory (AAOL)

In this work, the Airborne Aero-Optics Laboratory (AAOL) in conjunction with PROPS were employed to conduct turbulence profiling experiments. The primary objective of AAOL is to provide an in-flight testing platform where aero-optics experiments can be performed under real conditions. AAOL campaigns have been an integral part of advancing current understanding of the aero-optical interactions associated with turrets as well as AO systems. Common data collected include high bandwidth wavefront time series and residual beam jitter measurements [7]. These experiments have the flexibility of being conducted at varying Mach numbers, Reynolds numbers, and altitude. As the research emphasis transitions to beam control (AAOL-BC), it has been recognized that accurate slant path turbulence profiling remains a fairly uncontested problem and has high relevance to many optical systems. For completeness in the overarching AAOL initiative, turbulence profiling studies using the AAOL-BC research platform are conducted. The objective was to measure path resolved atmospheric turbulence quantities and compare with models such as HV57, ubiquitous in literature.

B. Path Resolved Optical Profiler System (PROPS)

PROPS is a product developed and provided by *MZA Associates Corporation*. The software and hardware supplied with PROPS allows for collection of DDTV statistics and real-time calculation of turbulence parameters such as C_n^2 *(z)*, Rytov parameter, Fried parameter, isoplanatic angle, Greenwood frequency, and Tyler frequency. Historically, measuring parameters such as C_n^2 *(z)* has been challenging. PROPS offers great promise in acquiring path resolved turbulence measurements with comparative ease. For this experiment, a double-sided configuration is used which enables the entirety of the propagation path to be approximated using the DDTV algorithm. Consequently, a double-sided PROPS data acquisition requires that both sides of the propagation path (ground side and air side) be equipped with sources, acquisition, and tracking systems. The following sections will discuss these setups in greater detail. For this experiment, turbulence profiles were collected in Coopersville, MI. This location was selected because it offered more than 300° of clear line of sight along the propagation path as well as logistical convenience.

C. Ground Station Setup

The PROPS ground station was equipped with blue and red LEDs, divergent light sources separated by 15.24 cm. The system also includes an infrared signal beacon allowing the air station to easily detect and track the ground station. The LED sources, track beacon, along with a wide field of view (WFOV) track camera are mounted next to a 203.2 mm Meade acquisition telescope, all of which are installed on a Meade LX200 gimbal mount. Here, the LED sources must be aligned prior to setting up the experiment. A narrow field of view (NFOV) track camera and a color SHWFS are connected to the back of the 203.2 mm telescope. The gimbal mount is manually adjusted to locate the distant target light sources. Once the target is within the WFOV, the tracking algorithms are engaged. Greater detail on the tracking algorithm will be discussed in a later section. Once the system is tracking and the telescope is focused on the air station sources, the exposure and iris are tuned allowing the appropriate amount of light intensity to the SHWFS. Specifications for the SHWFS used are presented in Table 1. A GUI, which comes with the PROPS software, enables the user to adjust exposure, verify SHWFS centroids, and alter acquisition settings. The ground setup in Coopersville, MI can be seen in Fig. 3.

Figure 3. Ground station setup in Coopersville, MI.

Table 1. SHWFS Specifications.

Wavefront Sensor Specifications	
Telescope Focal Length	2048 mm
Collimating Lens Focal Length	30 mm
Magnification	68.27
WFS Camera	FLIR Grasshopper 3, GS3-U3-23S6C-C
Operating Resolution	400x400 Pixels
Camera Pixel Size	11.72μm
Operating Frame Rate	200 fps
Lenslet Pitch	150 μm
Lenslet Focal Length	6.7 mm
Subaperture Pitch	12.79 Pixels

D. Air Station Setup

For double-sided profiling, the source, acquisition, and tracking systems were also installed on the aircraft. Implementing PROPS into an AAOL aircraft had associated challenges. Namely, space and size limitations required that the sources be injected through the telescope. Rather than LED sources, two fiber laser sources (blue and red) collimated to 5 mm were injected through the 203.2 mm Celestron telescope and out of the aircraft window. This method also avoided obscuring the telescope (with system hardware) dually used for acquisition of light received from the ground station. The system configuration installed in the aircraft is illustrated in Fig. 4. The incoming light from the ground station enters the aircraft through the optical window where it is then reflected off an AOM360 AeroTech Gimbal. A tracking mirror allows light to pass on through to the telescope while a FLIR camera with a Nikon lens also serves as the WFOV track camera. After passing through the telescope, the light is partitioned between a color SHWFS and an AVT GoldEye SWIR NFOV track camera.

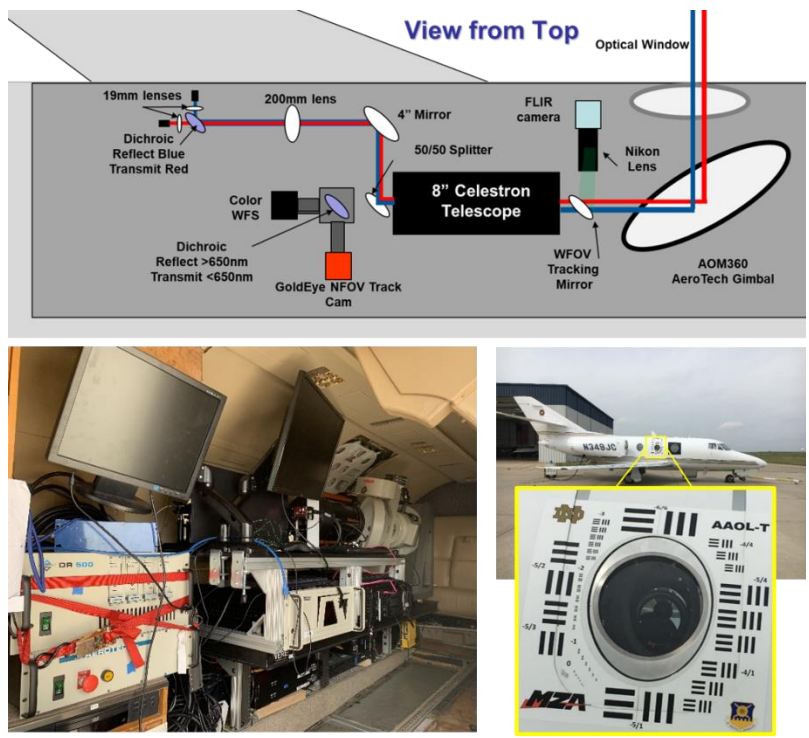

Figure 4. Air station setup in AAOL aircraft.

E. Tracking Systems

Tracking on both ends of the propagation path is necessary for data acquisition making the smooth operation of both air and ground systems required for a successful campaign. Tracking algorithms were supplied by *MZA Associates Corporation*. The ground station was stationary in an open field. For the ground station using the Meade LX200 gimbal, the system was able to maintain track approximately 80% of each orbit with both WFOV and NFOV tracking engaged. Tracking conditions on the air side were more susceptible to environmental conditions such as changes in altitude and cloud cover. For the air side, the operator would manually acquire the target in the WFOV, engage tracking, and then transition to NFOV. The air station was able to successfully acquire and maintain track for approximately 50% of each orbit. Snapshots from the tracking video for both the air and ground side can be seen in Fig. 5

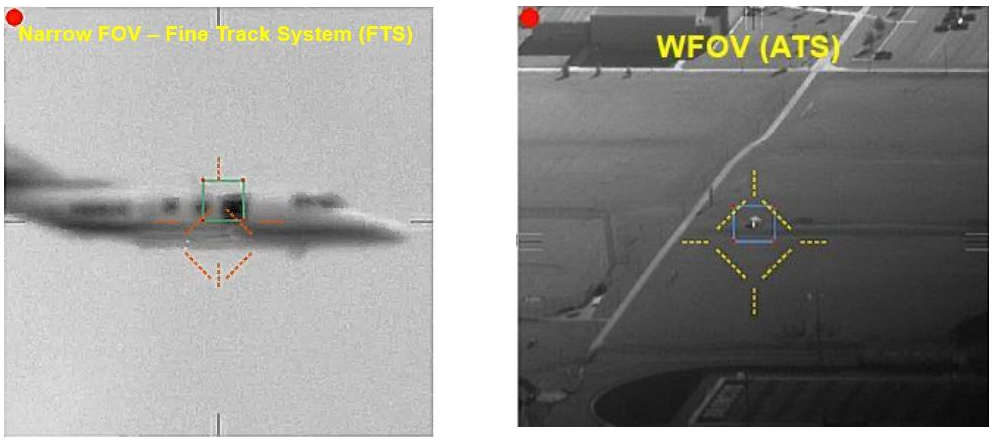

Figure 5. Left) Tracking on the ground station (NFOV). Right) Tracking on the air station (WFOV).

F. Acquisition Procedure

The aircraft flew programmed orbits continuously around the ground station terminal at an altitude of nominally 2.1 km. The ground radius of the orbit was approximately 7.4 km, giving a propagation slant path of approximately 8 km. The geometry of each orbit was recorded using a Trimble GPS. The altitude of cloud cover, Sun's position, and wind conditions dictated any deviations from this flight plan. Radio communication allowed for conversing between the ground and air teams. The data collected from the campaign was organized by orbit number. Data collection was initiated in the Southeast and ended in the Northeast of the orbit. An aerial view of the orbits is presented in Fig 6.

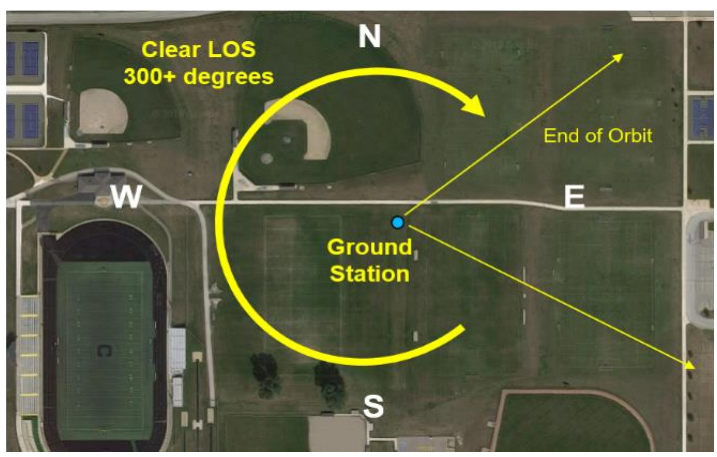

Figure 6. Orbit schematic.

G. Data Processing

Unlike SHWFS data collected by two stationary terminals, the challenge of data processing with a mobile terminal lies in filtering out erroneous data caused by changing flight conditions. This section summarizes the procedure, functions, and inputs required to convert the raw data acquired in these campaigns, into meaningful turbulence measurements. The raw data are image files from the SHWFS acquired from the blue and red light sources, at both ends of the propagation path. When the pointing between the air station and the ground station is ideal, the raw SHWFS

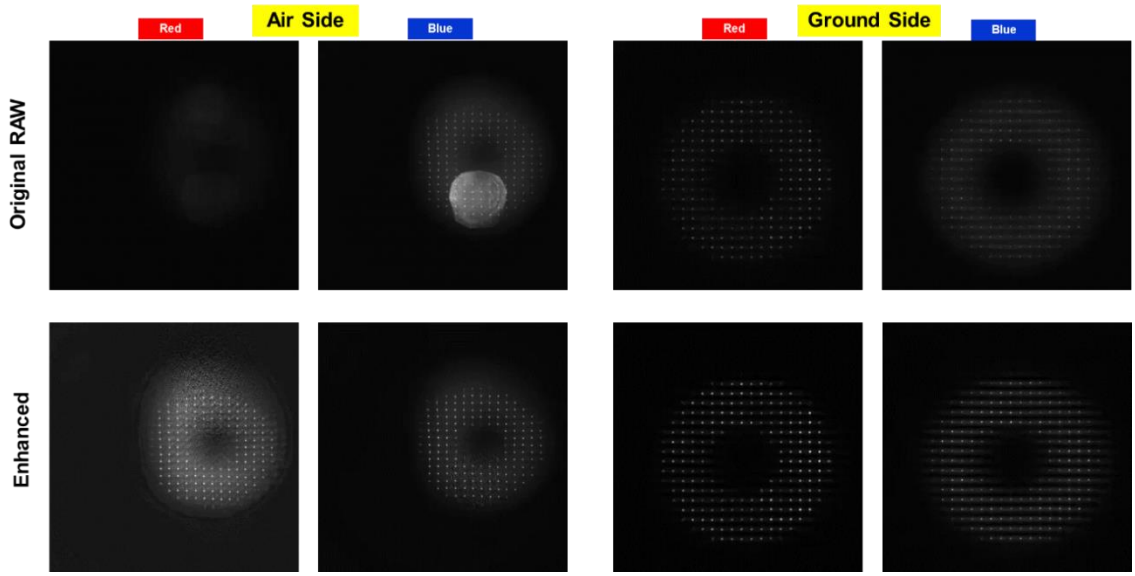

Figure 7. WFS imagery from both air and ground stations.

images look similar to typical stationary terminal data. When the pointing error exceeds 0.5 mRad at either terminal (ground station or air station), the light source signals are lost which results in acquisition of only background light by the cameras. The amount of background light was dictated by the size of the system iris, which for these experiments, was typically set to between 2 and 4 mm. The ground station looking into the sky experiences higher background levels in the blue channel. The air station observed less ambient background signal looking down towards the ground. In addition to mis-pointing, erroneous data is triggered by solar glints, telescope clipping, and source back reflections. Solar glints appear as bright sources which saturate the camera, inhibiting SHWFS slope calculations. Telescope clipping is an issue primarily on the air terminal side. The air system could tolerate pointing adjustments up to 0.5° in azimuth and 3° in elevation without clipping on the aircraft window. If wind altered the orbit, the 0.5° limit in azimuth would be exceeded resulting in left/right clipping. If the bank angle of the aircraft fluctuated more than 3°, the air terminal would experience up/down clipping. Lastly, on the air side, there are several optical components that could have back reflection such as the aircraft optical window, the front glass surface of the 8” Celestron telescope, or the 50/50 splitter positioned behind the telescope. These components are illustrated in Fig. 4. Ideally, these components should have 100% transmittance. Due to the various sources for potential erroneous data as well as the unpredictable and unavoidable nature of some of these challenges, the teams opted to continuously collect all

SHWFS data and sort between valid and invalid data in the post-processing procedure, described in Fig. 8.

The recorded data files are analyzed based on intensity thresholds defined by the user. The user defines values for the minimum and maximum pixels above threshold requirements for the valid imagery. If the pixels above the threshold value are too low, there will not be enough illuminated subapertures. Conversely, if the pixels above the threshold value are too high, we are likely observing only background or a glint. Example imagery from both the air and ground stations is presented in Fig. 7. In order to have a continuous data sequence for profile processing, a minimum number of consecutive frames that meet the number of pixels above threshold criteria is chosen. If a set of continuous frames met these conditions, this sequence is saved for further processing. For the data collected during this campaign, sequences consisting of at least 2.5 seconds (500 frames) of uninterrupted valid data were selected. Once "good" sequences are identified, an algorithm is used to identify the subaperture regions within the imagery and extract centroid slopes. From here, global tilt is removed and the data is formed into a structure that can be used to calculate DDTV statistics. The GPS logs from the Trimble are required to set the exact geometry of the test environment. Once the correct format is established, the data is run through the DDTV algorithm. Data points are put into bins based on subaperture separation. These separations will ultimately correspond to the number of relevant statistics associated with each weighting function. The algorithm iterates until convergence is achieved and a profile of $C_n^2\ (z)$ versus propagation distance is generated. A step-by-step flow diagram of the data processing procedure is depicted in Fig. 8.

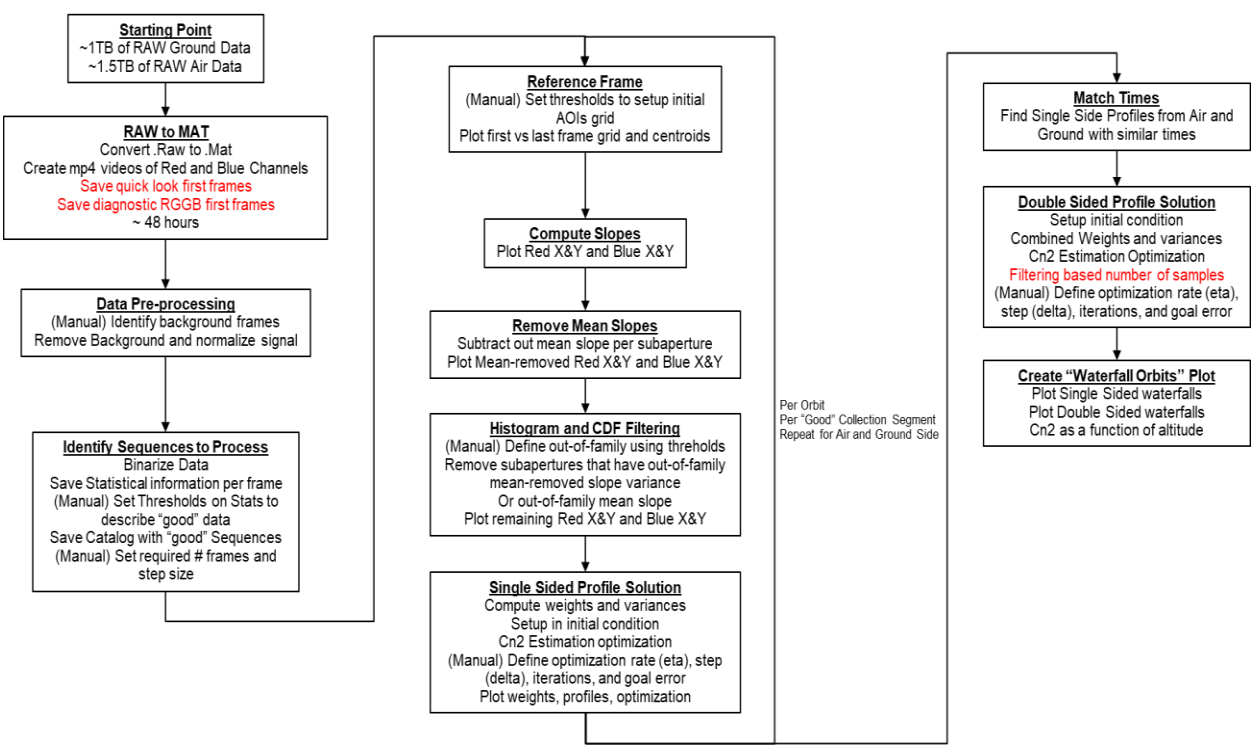

Figure 8. Data processing flow chart.

IV. Results and Discussion

PROPS generates single-sided profile solutions measured by each terminal. For every SHWFS data sequence that passes the filtering process, described in Sec. 3.7, PROPS outputs a 30-bin solution. In order to get a double-sided profile, collection times must be matched to identify valid sequences that occurred simultaneously on the air station and at the ground station. The sections below describe the key differences between single-sided and double-sided profiling solutions.

A. Single-Sided Profiles

For these turbulence profiling flight campaigns, data is collected at each end of the propagation path and single-sided profiles can be generated. Due to the relative source separation distance (~15 cm) versus subaperture separation distance (~19 cm), single-sided profiles do not provide DDTV weighting functions on the side of the propagation path closest to the sources, or farthest from the acquisition station. Single-sided profiles are independently generated for both the air and ground station data, as seen in Fig. 9. The DDTV data collected by the air station resolves the portion of the path closest to the aircraft whereas the ground station resolves the lower half of the propagation path, as shown by the weighting functions in the bottom plots of Fig. 9. Double-sided profiles are generated by using statistics from both stations, at the same acquisition time. Here, the plot on the bottom right illustrates how the weighting functions now more accurately resolve the entirely of the path, and the corresponding $C_n^2\ (z)$ profile can be seen in the top right plot of Fig. 9.

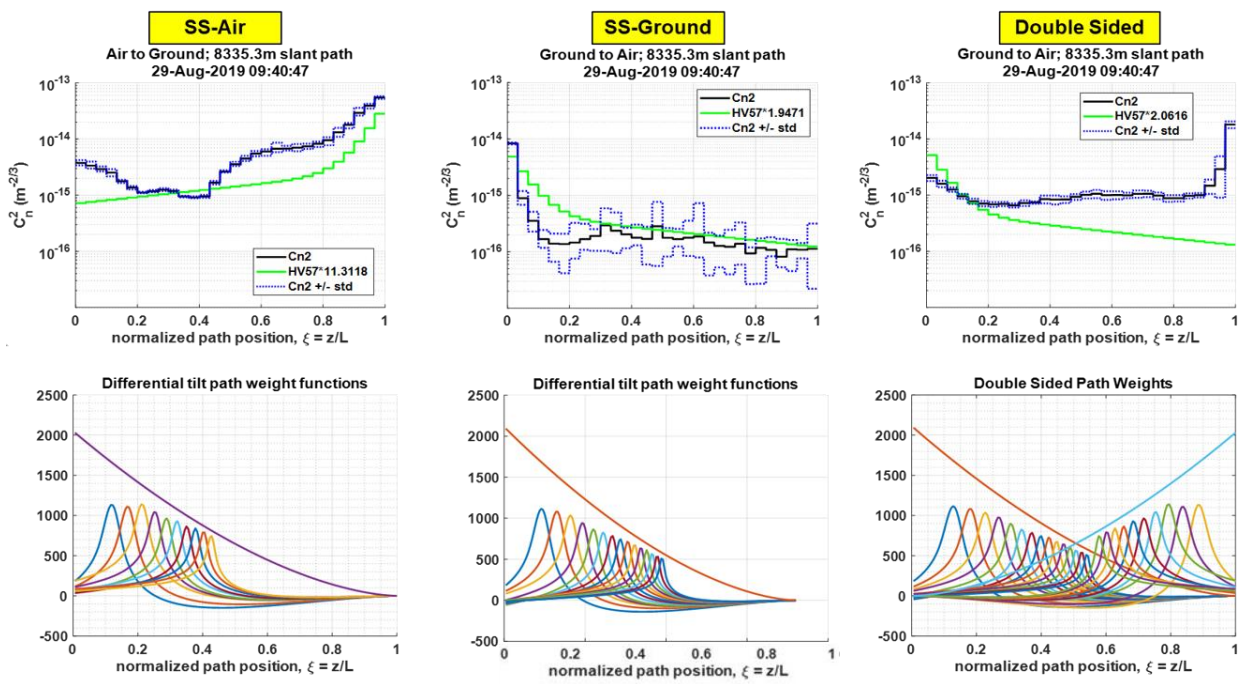

Figure 9. Comparison of single-sided profiles to double-sided profiles.

B. Double-Sided Profiles

The data collected during these campaigns seeks to accurately resolve the full slant path. Therefore, the double-sided profiles are the primary interest. Fig.10 presents the process for generating a double-sided profile, given a set of pre-processed, air and ground DDTV statistics taken at the same acquisition time. From the figure in the top left, the blue and red bars represent the DDTV values corresponding to ground and air station data, respectively. The magnitude of the $\sqrt{DDTV}$ is presented in terms of μRad. From this plot, the influence of the individual weighting functions is assessed. The example shown contains 15 weighting functions from the ground station and 6 weighting function from the air station. The number of weighting functions available comes from the SHWFS data and the number of subaperture separations available. In this example, the air side data does not include long subaperture separations. Consequently, the weighting functions from the air side do not extend out into the middle of the slant path. The corresponding weighting functions and their location along the propagation path are shown in the top right plot of Fig. 10. The profiling solution algorithm iterates until converged. The error metric from the stochastic parallel gradient descent (SPGD) optimization algorithm [27] used to determine convergence is presented in the bottom left plot. This plot shows that the optimization error flattens out after 100,000 iterations and a minimal error is reached. Ideally, the optimization algorithm would find an absolute minimum in the profile solution, but optimization parameters (learning rate, step size, number of iterations) were selected to provide sufficient outputs for a large variety of input DDTV statistics. The output profile solution of the algorithm is shown in the bottom right plot. This plot contains the profile initialization curve in pink, which corresponds to $\alpha \times HV57$. The scaling factor, α, is computed from the measured r_0 and the spherical wave r_0 corresponding to an $HV57$ atmosphere. The scaling factor, α, is defined as

$$\alpha = \left(\frac{r_0^{PROPS}}{r_0^{HV57}}\right)^{-5/3} \tag{9}$$

$$r_0^{PROPS} = \frac{(r_0^A + r_0^B)}{2} \tag{10}$$

The r_0^{HV57} is computed for a visible wavelength, $\lambda = 532\text{nm}$. The r_0^A is the measured r_0 for the ground station, computed by averaging the measured r_0 in the red and blue channel of the SHWFS. Similarly, the r_0^B is the measured r_0 for the air station computed by averaging the measured r_0 in the red and blue channel of the SHWFS. Eq. 10 shows that the measured r_0^{PROPS} is an average of the r_0^A and r_0^B from the ground station and air station terminals, respectively.

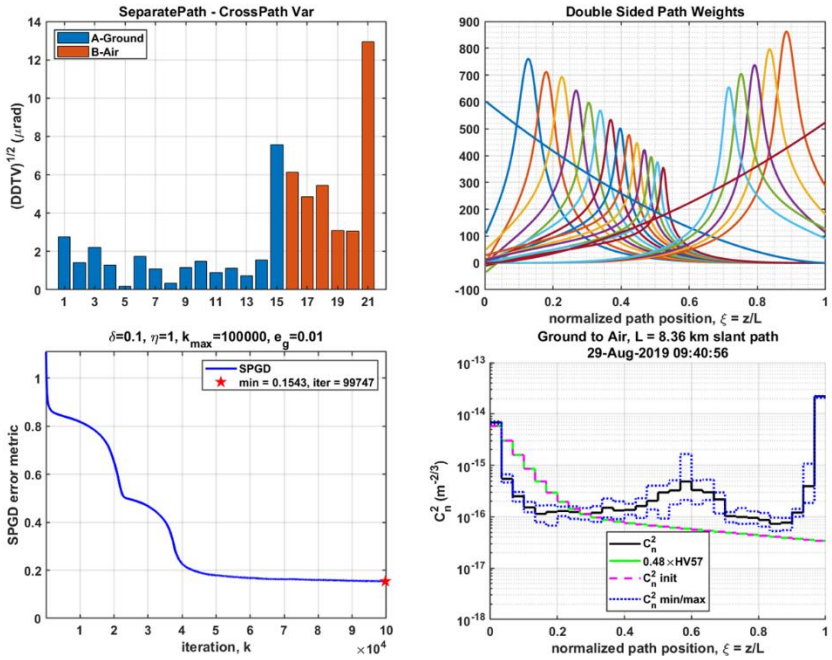

Figure 10. DDTV inputs, weighting functions used, profile solution optimization curve, resulting profile.

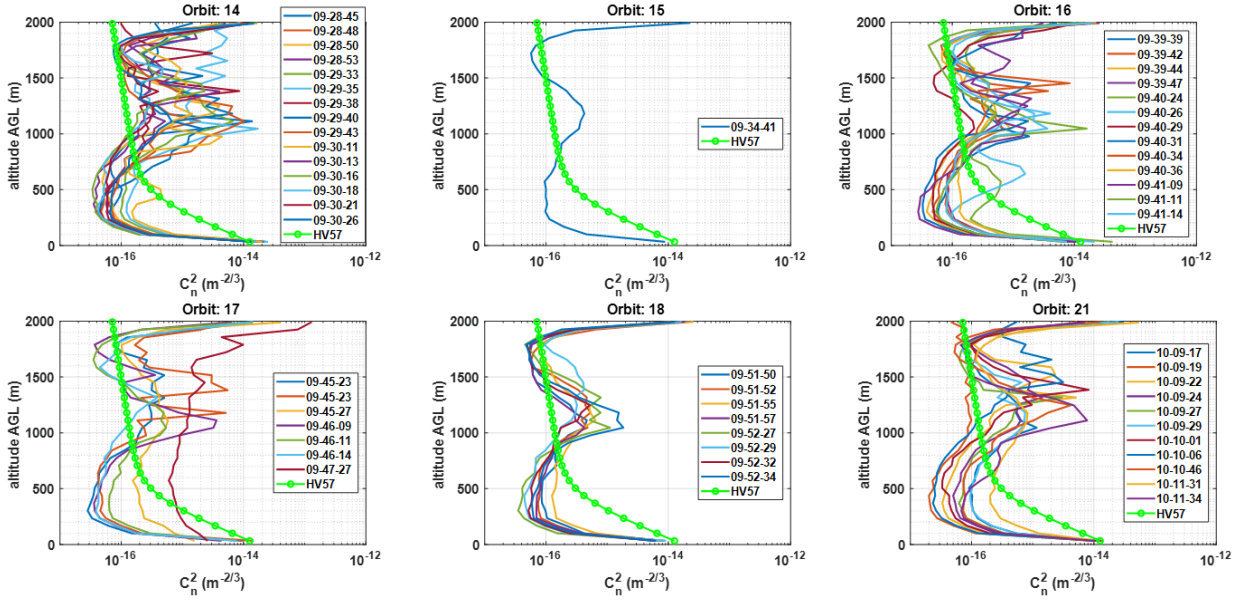

Figure 11. Turbulence profiles for six orbits.

Turbulence profiling results obtained from the PROPS flight campaign, recorded between 9:28 a.m. and 10:12 a.m. are shown in Fig. 11. Here, C_n^2 *(z)* is plotted versus altitude above ground level (AGL) for different orbits and the data lines on each plot correspond to collections that took place at different times within each orbit. For comparison, the widely used HV57 model is also plotted as a green line with circle markers. It can be seen that at the ground (altitude AGL ≈ 0m), the empirical data and the HV57 model are in agreement. However, the measured values show that C_n^2 *(z)* decreases from 1x10^{-14} to 1x10^{-16} m$^{-2/3}$ about 100 m off the ground whereas HV57 predicts a more gradual decrease in turbulence strength with altitude. In general, HV57 tends to overpredict the turbulence strength at low altitudes. Interestingly, at the highest altitude corresponding to the data collected next to the AAOL aircraft (altitude AGL ≈ 2,000m), there exists a seemingly spurious spike in turbulence strength. Current atmospheric models do not predict a drastic turbulence intensity rise at these altitudes like what is seen in the measured data. The presumption is that the aerodynamic turbulence associated with the plane propagating through the atmosphere imposes localized distortions onto the incoming light. Therefore, the spikes in turbulence strength seen above approximately 1750 m are not believed to be attributed to atmospheric turbulence, rather, they are due to aero-optical effects caused by the boundary layer over the aircraft window.

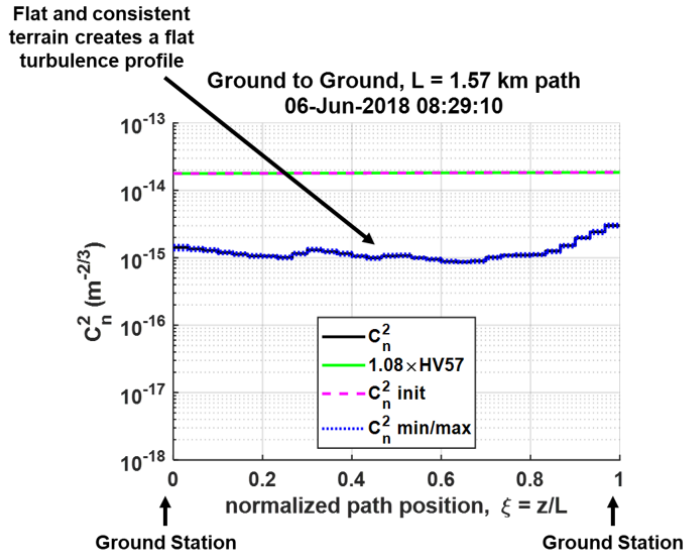

Figure 12. Turbulence profile for a ground to ground propagation path.

For comparison, a double-sided turbulence profile collected using the PROPS system for a ground to ground traverse is shown in Fig. 12. There was no significant change in terrain or altitude which correspondingly, produces a turbulence profile that remains fairly constant across the propagation path. It is clear, that the phenomena seen in the air to ground experiments is not present here. Also seen in the air to ground turbulence profiles is a significant increase in C_n^2 *(z)* between 1000 to 1500 m altitude AGL, where HV57 seems to underpredict turbulence strength. It is difficult to make conclusive statements about the reasons for the turbulence enhancement between 1000 to 1500 m altitude AGL, but one reasonable hypothesis is that the measurements are capturing the turbulent effects of the Earth boundary layer. This spike in C_n^2 *(z)* is followed by a decay in turbulence strength which converges to a value in agreement with HV57 between altitudes of 1500 and 1700 m.

C. Environmental and Operational Findings

The AAOL aircraft used for experimentation has a conformal, optical quality window installed. Using a conformal window indicates that there exists a preferential angle to look through for best optical quality. Consider the illustrations presented in Fig. 13. The black ovals represent the aircraft

fuselage and the blue line bisecting these ovals represents the angle of the wings. With respect to the horizontal plane of the wings, the installed window forms an angle of 70.76°. The conformal optical window was originally designed for a different window location in the fuselage with a slightly different viewing angle. The ideal angle to look through the conformal window is 67.5° with respect to the horizontal plane of the wings. This is illustrated by the diagrams indicated *a* and *b* in Fig. 13. Since the optical window sits lower in this experiment than originally designed, there is 3.26° difference between the ideal viewing/operation angle and the optical axis of the conformal window. Therefore, the preferred, more optically ideal scenario is to look down at a greater angle towards the ground station. Fig 13*c* shows that at this configuration the PROPS optical axis and the gimbal optical axis would need to be positioned above the center of the window to allow the operational pointing to be centered around the 3.26° downward looking angle. Having the PROPS optical axis positioned higher would allow us to center the operation on the optical axis of the conformal window. Fig. 13*d* shows that the bank angle of the AAOL aircraft varied between 12° and 20° depending on the wind conditions. As shown in Fig 13*e*, this creates challenging conditions in which the gimbal has to correct for ±4° of pointing elevation. The selected position and angle for PROPS in this campaign turned out not to be on the optical axis of the conformal window, thus the FTS imagery experiences optical distortion based on varying parts of the conformal window.

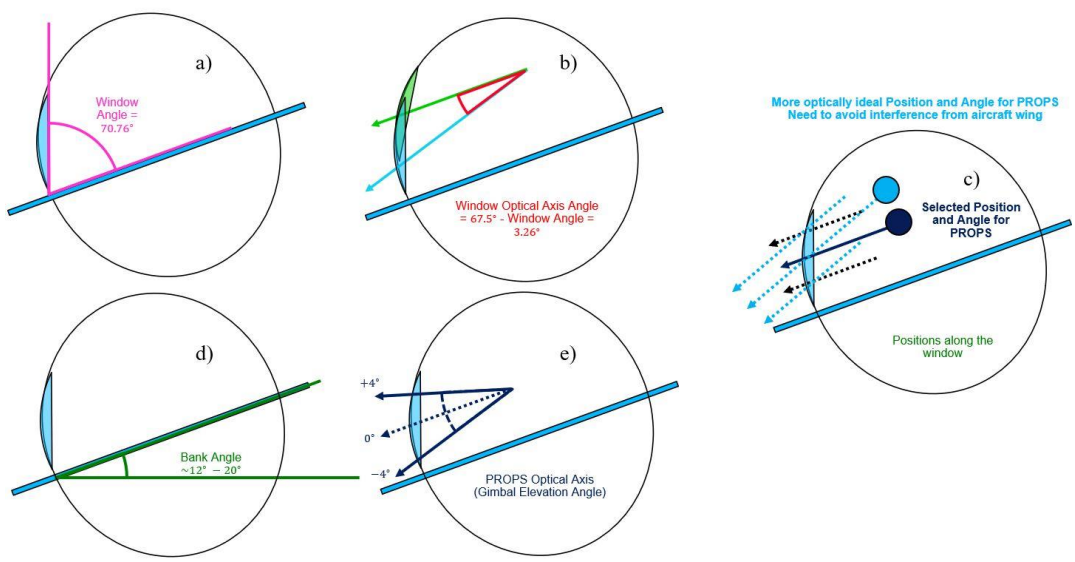

Figure 13. Optical axis in conformal window.

Based off the orbit radius and altitude of interest for this campaign, the flight speed and bank angle were set to 280 knots and 16°, respectively. However, the bank angle and speed of the aircraft changes throughout the orbit to accommodate and compensate for the wide range of environmental conditions. During the time of the campaign, winds were reported out of the West at 30 knots. Consequently, flying with the wind resulted in flying at a higher true ground speed and flying into the wind resulted in flying at a lower true ground speed. In order to maintain the same orbit, the bank angle was changed to compensate for the flight speed. This is best illustrated

in Fig. 14. Here it can be seen that in the North, where the aircraft was flying with the wind, the bank angle increased from 16° to 19°. Therefore, the AeroTech gimbal installed in the aircraft needed to respond by looking through a higher part of the conformal window (in the opposite direction from the optical axis of the conformal window which is 3.26° downward). Conversely, in the southern part of the orbit, the aircraft flew at a bank angle of 13° to accommodate for the slower flight speeds. In this scenario, the gimbal responds by looking down more on the conformal optical window (and closer to the ideal optical axis of the conformal window). Also shown in Fig. 14 is imagery corresponding to different orbit positions. The images taken in the southern part of the orbit are the clearest. Based on the previous discussion, this is due to looking through the conformal window at a more optically ideal angle. However, having this lesser bank angle prevented the collection of PROPS data due to clipping of the ATS WFOV camera. Fig. 14 also shows the alignment of the 8" PROPS aperture with respect to the window at different parts of the orbit. The window alignment in the North, East, South and West parts of the orbit is illustrated. The blue circle represents the 8" Celestron used for the PROPS measurement, and the red dashed lines show the center of the window. This indicates that in the West and East parts of the orbit our pointing was directly out the center of the window. The reported East and West part of the orbit's elevation angles (shown in yellow) are 0.3° and -0.6°, respectively. For reference, 0° elevation is aligned with the center of the window and -3.26° is the ideal optical axis of the window. In the northern part of the orbit, the telescope is looking through the upper part of the window. The corresponding elevation angle is +3.8° (~7° away from the ideal optical axis of -3.26°. In the southern part of the orbit, the elevation angle is -3.2° and closest to the ideal -3.26°, which as previously mentioned, results in the clearest imagery. Reiterating, this part of the orbit does however induce clipping preventing the acquisition of PROPS data. The imagery seen in the North was significantly blurrier but permitted PROPS data to be collected.

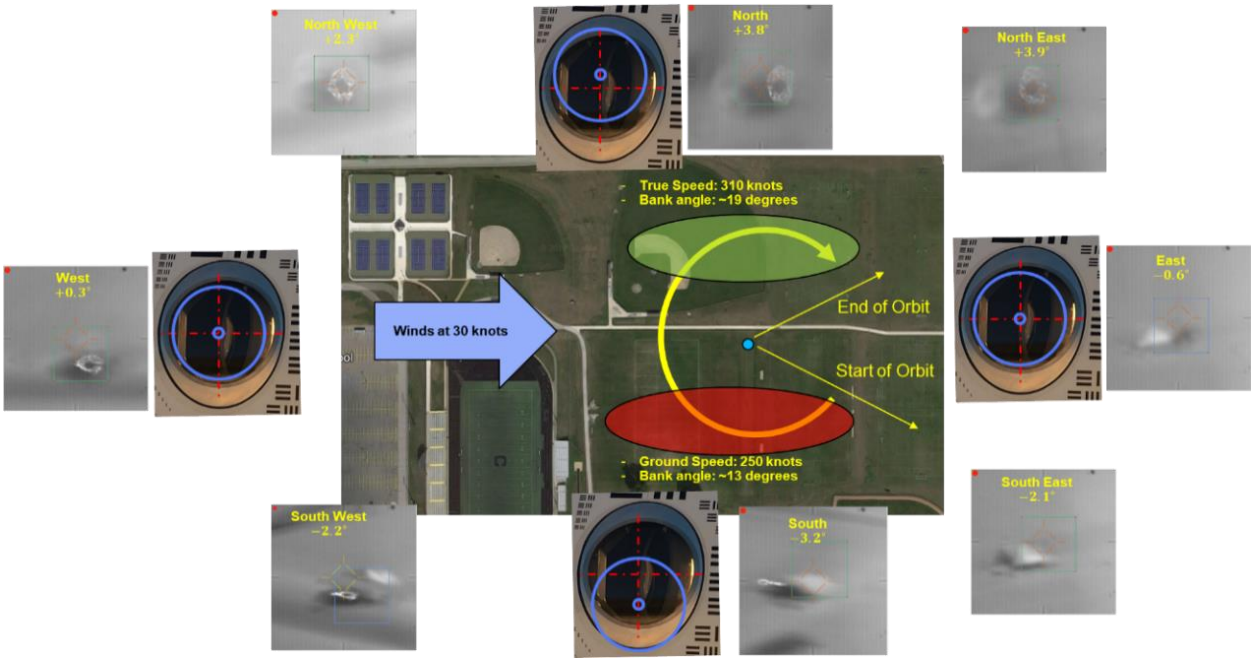

Figure 14. Optical axis based on orbit position.

A more detailed look at how the environmental conditions caused a deviation from the flight plan can be seen in Fig. 15. These plots illustrate how slant path length and cruise speed were changed as a function of orbit position. These results were obtained by analyzing the Trimble GPS 10Hz data. In Fig. 15, the plot on the left shows the changing slant range. Interestingly, the maximum slant range is to the Northeast part of the orbit. With 30 knot wind out of the West, one would expect the orbit to become elongated, west-to-east. However, the slant range plot does not show that. In fact, surprisingly, the recorded orbit remains very much circular. The wind did cause the center of the orbit to shift to the Northeast, but only by ~150m. We attribute the Northeast elongation (instead of the expected directly East elongation) due to the autopilot software corrections. The system would sense the acceleration due to the wind from the West then start to apply corrections to the speed and bank angle to stay in the designated orbit. In Fig 15, the right plot shows how the true ground speed of the aircraft changed throughout the orbit. The speed plot is more intuitive when considering the wind out of the West. Here, it can be seen that the highest aircraft speed (160m/s) is in the northern part of the orbit. Conversely, the southern part of the orbit is slowest at 130m/s.

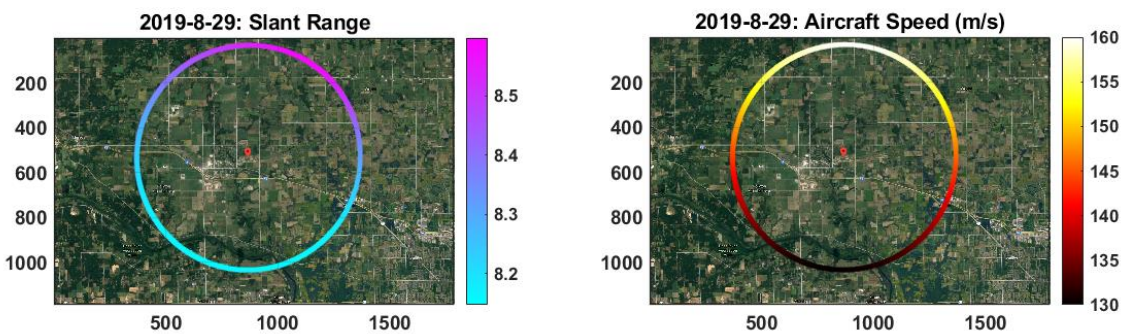

Figure 15. Slant path length and aircraft speed v. orbit position.

Based on these findings, future experimentation will make use of a flat optical window. This implementation will alleviate the issue of preferred optical quality angles. An affirmation of this is presented in Fig. 16. Imagery was taken through both the conformal window and a flat window at different angles. The conformal window has only a narrow region of angles that yielded clear images, whereas the flat window image quality is independent of angle for the ranges tested. The FTS image quality with the conformal window significantly changed based on viewing angle deviations of even ±4°. With the flat window, we expect to have global tilt but significantly less image distortion.

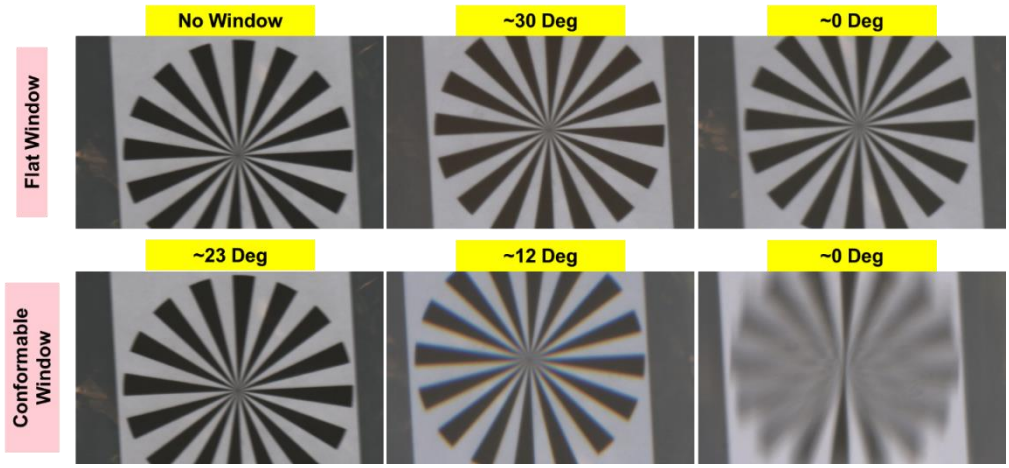

Figure 16. Flat v. conformal window at varying look through angles.

V. Conclusions

The work presented here demonstrated how PROPS in conjunction with AAOL can be used for turbulence profiling measurements. Results were presented that show agreement with current models such as HV57, commonly referenced in literature. Deviations of the calculated profiles away from models, affords an exciting opportunity to further examine interesting physics which may have been previously overlooked. The measured turbulence profiles showed consistently lower values of C_n^2 *(z)* close to the ground indicating that HV57 is overpredicting turbulence intensity. However, at altitudes between 1000 to 1500 m, the measured values of C_n^2 *(z)* were higher than what the HV57 model predicts. This increase in turbulence strength captured by PROPS at altitudes above 1 km warrants further investigation. It was also noted that in the region close to the aircraft, higher levels of turbulence strength were reported. It is believed that this spike in C_n^2 *(z)* is attributed to the aero-optical effects caused by the boundary layer over the aircraft and not imposed by atmospheric turbulence. Future work seeks to employ novel approaches to decouple these phenomena. This work also discussed some of the associated challenges with the praxis and implementation of PROPS on a flight vehicle. Whilst a successful measurement campaign, we continue enhancing the capabilities of a slant path profiling system and identifying the requirements, limitations, and best practices moving forward.

VI. Acknowledgments

This work is supported by the Joint Technology Office, Grant number FA9550-13-1-0001 and Office of Naval Research, Grant number N00014-18-1-2112. The U.S. Government is authorized to reproduce and distribute reprints for governmental purposes notwithstanding any copyright notation thereon.

VII. References

1. Fried D.L., "Optical Resolution Through a Randomly Inhomogeneous Medium for Very Long and Very Short Exposures," Journal Op. Soc. Am., 56-10, October 1966.
2. Andrews L., Phillips R., *Laser Beam Propagation Through Random Media,* SPIE-International Society for Optical Engineering, 2005.
3. Jumper, E.J., Zenk, M., Gordeyev, S., Cavalieri, D., and Whiteley, M., "Airborne Aero-Optics Laboratory", Journal of Optical Engineering, 52(7), 071408, 2013.
4. Gordeyev S., Jumper E., "Fluid Dynamics and Aero-Optical Environment Around Turrets," AIAA 2009-4224.
5. Gilbert K.G., Otten L.J., "Aero-Optical Phenomena," Progress in astronautics and aeronautics series, Vol. 80. New York: American Institute of Aeronautics and Astronautics, 1982.
6. Sutton, G.W., "Aero-Optical Foundations and Applications," AIAA Journal, Vol. 23, pp. 1525-1537, 1985.
7. Porter C., Gordeyev, S., Zenk, M. and Jumper, E.J., "Flight Measurements of the Aero-Optical Environment around a Flat-Windowed Turret," AIAA Journal, 51(6), pp. 1394-1403, 2013.
8. De Lucca, N., Gordeyev, S., and Jumper, E., "In-flight aero-optics of turrets," Journal of Optical Engineering, 52(7), 071405, 2013.
9. J. Morrida, S. Gordeyev and E. Jumper, "Transonic Flow Dynamics Over a Hemisphere in Flight," 54th AIAA Aerospace Sciences Meeting, 4 - 8 Jan 2016, San Diego, California, AIAA Paper 2016-1349.
10. Tatarski V.I., *Wave Propagation in a Turbulent Medium*, McGraw-Hill Book Company, 1961.
11. "Kolmogorov Theory of Turbulence-Atmospheric Optics." *SPIE,* 28 December 2018, https://www.spie.org/samples/FG02.pdf.
12. Whiteley M.R., "Rytov Parameter Estimation by use of Differential-Tilt Measurements," Proc. SPIE 4125, Propagation and Imaging through the Atmosphere IV, (17 November 2000); doi: 10.1117/12.409299, 2000.
13. Oesch D.W., Sanchez D.J., et al., "The Aggregate Behavior of Branch Points- Branch Point Density as a Characteristic of an Atmospheric Turbulence Simulator," SPIE, San Diego, CA, 377ABW-2009-1028 August 5, 2009.
14. Razdan A., "Measurement of atmospheric turbulence parameters relevant to adaptive optic system design," Proc. SPIE 4976, Atmospheric Propagation, (30 April 2003); doi: 10.1117/12.479215, 2003.
15. Eaton F.D., Peterson W.A., et al., "Comparisons of VHF Radar, Optical, and Temperature Fluctuation Measurements of Cn^2, r_0, and Θ_0," Theor. Appl. Climatol. 39,17-29, 1988.
16. VanZandt T.E., Green J.L., Gage K.S., Clark W.L., "Vertical Profiles of Refractivity Turbulence Structure Constant: Comparison of Observations by the Sunset Radar with a New Theoretical Model," *Radio Science*, 13-5, pg. 819-829, 9/1978-10/1978.
17. Fried D.L., "Remote Probing of the Optical Strength of Atmospheric Turbulence and of Wind Velocity," Nasa Technical Report, NAS-NRC Atmospheric Exploration by Remote Probes, Vol. 2 p 133-144 (SEE N72-25347 16-13).
18. Ottersten H., "Radar Backscattering from the Turbulent Clear Atmosphere," *Radio Science*, 2-12, pg.1251-1255, 12/1969.

19. Zink R., Vincent R.A., Murphy E., Cote O., "Comparison of Radar and In Situ Measurements of Atmospheric Turbulence," JOURNAL OF GEOPHYSICAL RESEARCH, VOL. 109, D11108, doi:10.1029/2003JD003991, 2004.
20. Cortes A., Neichel B., et al., "Atmospheric Turbulence Profiling Using Multiple Laser Star Wavefront Sensors," *Monthly Notices of the Royal Astronomical Society*, Volume 427, Issue 3, 11 December 2012, Pages 2089–2099.
21. Tyson, R.K., 2000, *Introduction to Adaptive Optics*, SPIE-International Society for Optical Engineering.
22. Andrews L., Phillips R., Young C.Y., 2001, Modeling Optical Turbulence, *Laser Beam Scintillation with Applications*, SPIE-International Society for Optical Engineering, https://doi.org/10.1117/3.412858.ch2.
23. Sasiela R.J., *Electromagnetic Wave Propagation in Turbulence*, Springer-Verlag, Berlin, 1994.
24. Noll R.J., 1975, "Zernike Polynomials and Atmospheric Turbulence," J. Opt. Soc. Am., Vol. 66, No.3, March 1976.
25. Whiteley M.R., "Optimal atmospheric compensation for anisoplanatism in adaptive-optical systems." PhD thesis, Air Force Institute of Technology, Wright-Patterson Air Force Base, Ohio, 1998.
26. Whiteley M.R., Welsh B.M., and Roggemann M.C., "Optimal modal wave-front compensation for anisoplanatism in adaptive optics," J. Opt. Soc. Am. A 15, pp. 2097—2106, August 1998.
27. Hasdorff, L., *Gradient Optimization and Nonlinear Control*, John Wiley and Sons, 1976.